

A RAMAN SPECTROSCOPY STUDY OF STEEL CORROSION PRODUCTS IN ACTIVATED FLY ASH MORTAR CONTAINING CHLORIDES

M. Criado,^{1*} S. Martínez-Ramírez,² J. M. Bastidas³

¹ Instituto de Ciencia de Materiales de Madrid, CSIC, Sor Juana Inés de la Cruz 3,
28049 Cantoblanco–Madrid, Spain

² Instituto de Estructura de la Materia, CSIC, Serrano 123, 28006 Madrid, Spain

³ Centro Nacional de Investigaciones Metalúrgicas, CSIC, Avda. Gregorio del Amo 8,
28040 Madrid, Spain

Abstract

Raman spectroscopy was used to characterise the corrosion products of reinforcing steel embedded in activated fly ash mortars in the presence of 0.4 and 2% chlorides. Two alkaline solutions with different soluble silica contents were utilised to activate the fly ash. Raman spectra were obtained using two excitation wavelengths (532 and 633 nm) and making power scans to select the suitable conditions of register for each wavelength. The main steel corrosion products identified were iron oxyhydroxides with low crystallinity, goethite (α -FeOOH) and lepidocrocite (γ -FeOOH). These products need to be studied using a spectrometer with the laser line of 532 nm at low powers from 0.025 to 0.25 mW or a spectrometer with the laser line of 633 nm at high power between 2.5 and 25 mW.

Keywords: Raman spectroscopy; Alkali activation; Fly ash; Iron corrosion products; Chloride

* Corresponding Author, Tel.: +34 91 334 9000; Fax: +34 91 3720623; E-mail Address: mcriado@icmm.csic.es (M. Criado)

Introduction

The degradation of reinforcing steel due to corrosion is of great concern for the durability of concrete structures and can lead to serious economic implications [1–3]. The most important causes of reinforcing steel corrosion initiation are the ingress of chloride ions and carbon dioxide to the steel surface. The depassivation of steel rebars can lead to the localised formation of porous oxide layers at the steel/concrete interface. The volume of iron oxide layers is two to four times larger than that of iron, and the high tensile stresses generated by the expansive volume of the corrosion products [4–6] can result in internal microcracking and spalling of the concrete cover. The rate of corrosion is a limiting factor of the remaining service life of a corroding reinforced concrete structure (RCS).

Therefore, the study and characterization of corrosion products in reinforced concrete is an important issue with a view to assessing the corrosion state within RCS and predicting their remaining service life. Several techniques like Raman spectroscopy [7], X-ray photoelectron spectroscopy (XPS) [8], Mössbauer spectroscopy [9], ellipsometry [10], secondary ion mass spectrometry (SIMS) [11], and atomic force microscopy [12] have been employed to study the passive film on the steel surface.

Micro-Raman spectroscopy is a preferred method because it is a non-destructive technique that is well suited for the in situ characterization of various oxides and oxyhydroxides involved in the corrosion of iron. Moreover this spectroscopy presents two important advantages: the lack of any need for sample preparation and the quick and easy obtainment of water/metal interface spectra [13–16].

Iron oxides and oxyhydroxides are known to be sensitive to thermal transformations even at low laser power because they are opaque to visible light and heat up. Indeed, a temperature rise induces a transformation to the most stable phase,

i.e. hematite (α -Fe₂O₃) [15]. As some iron oxides are highly sensitive to laser irradiation, several authors have used a set of density filters to modulate the laser power and avoid any thermal effect on iron (III) compounds [15,17–19].

De Faria et al. [20] employed Raman microscopy to investigate the laser power dependence of the Raman spectra of oxides and oxyhydroxides like hematite (α -Fe₂O₃), magnetite (Fe₃O₄), wüstite (FeO), maghemite (γ -Fe₂O₃), goethite (α -FeOOH), lepidocrocite (γ -FeOOH) and feroxyhyte (δ -FeOOH). The results obtained showed that increasing the laser power causes the characteristic bands of hematite to show up in the spectra of most of the studied compounds, with the consequent band broadening and shifts of the hematite spectrum. Under high laser power all the investigated oxyhydroxides showed the characteristic peaks of hematite, with the power threshold being dependent on the surface morphology.

Nieuwoudt et al. [21] demonstrated that significant enhancements of the Raman spectra for iron oxides and oxyhydroxides can be achieved using an optimised excitation wavelength of 636.4 nm, providing further improvement over those attained with the 632.8 nm excitation wavelength under similar conditions. When compared, the Raman spectra for standard iron compounds in the low wave number region ($<1000\text{ cm}^{-1}$) obtained using a tuneable dye laser with the 636.4 nm line are more intense and well-defined than those obtained using an excitation wavelength of 514.5 nm.

Taking into account all these premises, the main aim of this paper was to study the corrosion products formed on steel embedded in alkali activated fly ash (AAFA) mortars in the presence of chloride ions using a Micro-Raman spectrometer with two excitation wavelengths (532 and 633 nm) and making power scans to select the suitable conditions of register for each laser line. Since several oxyhydroxides can be formed as

corrosion product it is important to discern if they become from laser irradiation transformation or as corrosion products.

The choice of AAFA as cementitious matrix is due to the fact that this is being used in concrete for reasons related with environmental impact, economic sustainability and social responsibility [22]. The alkali activation of type F fly ash consists of mixing the fly ash with highly alkaline solutions ($\text{pH} > 13$) and subsequently curing the resulting paste at a certain temperature to produce a solid material. Considering that RCS safety and durability are two of the most important requirements for building protection, the capacity of an AAFA mortar to passivate steel rebars is a necessary property to guarantee both aspects of RCS constructed using these new materials.

Experimental

Concrete reinforcement electrodes were cut from carbon steel plates with a chemical composition of 0.45% C, 0.22% Si, 0.72% Mn, $<0.010\%$ P, 0.022% S, 0.13% Cr, 0.13% Ni, 0.18% Cu, and balance Fe. The specimen surfaces were polished with emery paper from 120 to 600, washed with double distilled water and degreased with acetone.

The cementitious material used was a type F fly ash (FA) from a coal-fired power plant at Aboño, Asturias, Spain. The chemical composition of the FA is shown in Table 1. The percentage of reactive silica (SiO_2) in the FA, determined according to UNE 80–225–93 standard [23], is 41.23% and the vitreous phase content is 65.60%. The procedure used to determine the vitreous phase content was similar to that described elsewhere [24]. Briefly, 1 g of FA was added to 100 ml of 1% hydrofluoric acid (HF) in a plastic beaker and stirred for 6 h at room temperature. The granulometry distribution, determined by laser ray diffraction, showed only one mode in which approximately 85% of particles were smaller than $45\text{ }\mu\text{m}$ and 50% smaller than $13\text{ }\mu\text{m}$.

The FA was activated using two different highly alkaline solutions with roughly the same sodium oxide (Na_2O) content ($\sim 20\%$) and varying proportions of soluble SiO_2 . The products used to prepare the solutions were laboratory grade reagents: sodium hydroxide (NaOH) pellets and waterglass (Na_2SiO_3) containing 27% SiO_2 , 8.2% NaOH , and 64.8% H_2O . One activating solution was prepared with 8M NaOH , and the other with 85% 10M NaOH and 15% waterglass.

Accordingly, two types of AAFA mortars were manufactured: one using the NaOH solution (FAA mortar) and the other using the 85% NaOH and 15% waterglass mixture (FAB mortar) with a “liquid/solid” ratio of 0.45. The mortars were prepared with sand/AAFA ratio of 2:1. The moulds containing the fresh AAFA mortars were cured in an oven at 85 °C in a saturated water vapour atmosphere for 20 h. Different amounts of sodium chloride (NaCl) (99% pure Panreac PRS–CODEX): 0.4 and 2% chloride (in relation to binder weight) were added to the FA. Two prismatic mortar specimens of each type, with dimensions 8 cm×5.5 cm×2 cm, were prepared for comparative purposes [25]. All the specimens were stored at room temperature in an atmosphere of high relative humidity (RH), $\sim 95\%$, for up to 720 days.

The steel was extracted from the FAA and FAB mortars and Raman spectra were obtained directly from the steel plate surface and analysed. Dispersive Raman spectra at 633 and 532 nm were recorded in a RM 1000 Renishaw Raman Microscope System. The Raman spectrometer is equipped with a Leica microscope and an electrically refrigerated CCD camera. The spectra were obtained with $\times 50$ magnification objective lenses. The final spectra were the result of 10 accumulations to improve the signal-to-noise ratio and the integration time was 10 s. The software employed for data acquisition and analysis was Wire for Windows and Galactic Industries GRAMS/32TM. Five scans were recorded to improve the signal-to-noise

ratio. The Raman shift was calibrated before the measurements according to the silicon peak at 520 cm^{-1} . The 633 nm line had a laser power from 0.25 to 25 mW and finally, the 532 nm line had a laser power from 0.0005 to 5 mW. The measurements were done directly in the sample (in situ), the sample preparation is not necessary.

Results and Discussion

Fig. 1 shows the steel specimens after extraction from the FA mortars in the presence and absence of chlorides for 720 days of experimentation. The steel specimens embedded in the mortars without chlorides present tiny amounts of corrosion products on a practically smooth surface, indicating that the steel was in the passive state in this new cementitious system. The steel specimens extracted from the chloride-polluted mortars present small fragments of the mortars on their surface and in some regions corrosion product layers are also observed. The amount of corrosion products formed was higher in the presence of 2% chlorides and the steel surface was fully coated in both FAA and FAB mortars.

The Raman spectra of iron oxides/hydroxides can be divided into two regions [26]: (i) $1200\text{ to }600\text{ cm}^{-1}$ for both Fe–O–H bending and Fe–O stretching vibration regions; and (ii) $600\text{ to }200\text{ cm}^{-1}$, this region includes absorptions overlapping of lattice vibrations as well as molecular frequencies. Fe–O stretching vibrations can also be absorbed below 400 cm^{-1} .

Fig. 2 shows Raman spectra of a corroded bar embedded in FAA mortar with 0.4% chlorides using an optimised excitation wavelength of 532 nm under different laser output powers. In the light regions, no compound was detected in the spectrum obtained with the laser power of 0.0005 mW, perhaps due to the use of a very low laser intensity. In the spectra recorded with 0.025 and 0.05 mW, two broad peaks around 695 (the most intense) and 1357 cm^{-1} were detected. These peaks were also observed for the

laser powers of 0.25 and 0.5 mW, along with other new peaks at 347, 541 and 1589 cm^{-1} . These bands are very broad, indicating the formation of corrosion products of low crystallinity, specifically iron oxyhydroxides [17,18]. Finally, when higher laser powers (2.5 and 5 mW) were employed, several sharp peaks typical of hematite were detected at 210 and 273 (very intense), 380, 478, 579 and 1274 cm^{-1} . The peak positions of this compound do not coincide exactly with those observed in other Raman spectra studies of iron corrosion products [13,18,19,21,27]. These differences may be due to the formation of “modified hematite”, which presents a structure with few changes or defects. The formation of modified hematite at 2.5 and 5 mW instead of the iron oxyhydroxides formed at a lower laser power may be due to the transformation of the corrosion phases under the higher laser heat during the measurements [5,20]. The spectrum for the steel embedded in FAA mortar with 0.4% chlorides obtained with a laser power of 5 mW also showed fluorescence, leading to an increase of the Raman intensity, (Fig. 2).

In the dark deposits on the steel surface, a power of 0.025 mW detected a series of well-defined peaks at 244, 300, 396 (the most intense), 476, 555, 682, 998, 1116 and 1309 cm^{-1} , indicating the presence of goethite [13,18,21,27]. This phase was transformed into modified hematite when the laser power was increased (2.5 mW), similarly to what happened in the light regions.

Fig. 3 shows Raman spectra for reinforcing steel embedded in FAA mortars with 0.4% chlorides using an optimised excitation wavelength of 633 nm under different laser output powers. In this case, the use of a lower energy laser (633 nm) with the powers of 0.25 and 2.5 mW allowed the detection of small peaks whose attribution was complicated. Therefore, these spectra were different to those obtained in the same conditions with the 532 nm laser (Fig. 2), where iron oxyhydroxides and hematite were

observed, respectively. Moreover, in the spectra recorded with laser powers between 6.25 and 25 mW, typical peaks of iron oxyhydroxides were detected which did not experience changes with the increase in laser power and where the phenomenon of fluorescence did not take place. In another area of the sample, goethite peaks were observed for all the range of powers. This phase was stable under a laser heat of 633 nm.

Fig. 4 shows Raman spectra of the corroded bar embedded in FAA mortar with 2% chlorides using an optimised excitation wavelength of 532 nm under different laser output powers. The spectrum obtained with the laser power of 0.0005 mW did not show peaks for iron compounds. On increasing the laser power (from 0.025 to 0.5 mW) a series of peaks typical of goethite were observed. The height and width of the peaks in the spectrum were higher and sharper respectively when the laser powers were raised (0.25 and 0.5 mW), and therefore the identification of goethite was easier. Major differences were observed in the spectra recorded for the steel embedded in FAA mortar with 2% chlorides at 2.5 and 5 mW, which presented several well-defined peaks detected at 215 and 276 (the most intense), 386, 484, 585 and 1296 cm^{-1} (Fig. 4), indicating the presence of hematite. The positions of these peaks were shifted, suggesting the formation of a modified hematite as occurred in the FAA mortars with 0.4% chlorides (Fig. 2). For 5 mW laser power the spectrum showed fluorescence and the peaks assigned to modified hematite lost intensity and definition.

Fig. 5 shows Raman spectra for the steel embedded in FAA mortars with 2% chlorides using an optimised excitation wavelength of 633 nm under different laser output powers. Iron corrosion products were not detectable in the spectrum recorded at 0.25 mW, but the formation of goethite was detected in the same spectrum with 532 nm the laser line. In this latter case, the presence of goethite was observed in the rest of the

spectra with laser powers between 2.5–25 mW. This longer wavelength (633 nm) did not lead to transformation of the compounds under laser heat (position of peaks remained fixed) or produce fluorescence during the measurements.

Fig. 6 shows Raman spectra of the corroded bar embedded in FAB mortar with 0.4% chlorides using an optimised excitation wavelength of 532 nm under different laser output powers. No peak was observed in the spectrum with the lowest power (0.0005 mW), but for laser powers of 0.025 and 0.05 mW two broad bands (1367 and 706 cm^{-1}) corresponding to iron oxyhydroxides were detected. In the spectra obtained at 0.25 and 0.5 mW, peaks were also observed at 1603, 523, 374 and 243 cm^{-1} (see Fig. 6). The peaks at 1603, 1367, 706, 523 and 374 cm^{-1} were assigned to oxyhydroxides with low crystallinity while the peak at 243 cm^{-1} was allocated to lepidocrocite [13,17,18]. The other lepidocrocite peaks at 1306, 523 and 374 cm^{-1} overlapped with the oxyhydroxides peaks. The intensity of these peaks increased with the power. However, at the laser powers of 2.5 and 5 mW these peaks disappeared and other peaks were located in the positions corresponding to hematite and modified hematite, respectively.

Fig. 7 shows Raman spectra for steel embedded in FAB mortars with 0.4% chlorides using an optimised excitation wavelength of 633 nm under different laser output powers. A series of peaks typical of lepidocrocite were detected for all the laser powers employed, but the power of 0.25 mW yielded only small peaks whose attribution was complicated. In the same sample lepidocrocite could not be detected as a single phase using the wavelength of 532 nm. The intensity of the lepidocrocite peaks increased with the power, but their position remained fixed, indicating that this laser line did not cause the transformation of lepidocrocite due to a heating effect as occurred in Fig. 6.

Fig. 8 shows Raman spectra for the corroded bar embedded in FAB mortar with 2% chlorides using an optimised excitation wavelength of 532 nm under different laser output powers. The spectra acquired with the laser powers of 0.0005 and 0.025 mW were similar that those obtained in the previous steel embedded in FAB mortar with 0.4% chlorides. Goethite was distinguished at 0.05 and 0.25 mW, showing peaks at 1313, 1122, 991, 689, 544, 479, 396 (the most intense), 300 and 247 cm^{-1} , whose intensity increased with the laser power. In the spectrum recorded using 0.5 mW new peaks were detected at 1313, 670, 400, 291 and 221 cm^{-1} , typical of hematite iron compound. In this phase the transformation of an iron compound to hematite occurred at a lower power (0.5 mW) than in the other samples. The positions of hematite Raman peaks were shifted to lower wavenumbers for higher powers (2.5 and 5 mW), indicating the presence of modified hematite. The spectrum obtained with 5 mW showed fluorescence and the resolution of hematite peaks was very low.

Fig. 9 shows Raman spectra for steel embedded in FAB mortars with 2% chlorides using an optimised excitation wavelength of 633 nm under different laser output powers. Small peaks were visible in the spectrum with 0.25 mW for the light regions on the steel surface, see Fig. 9(a). The intensity of these peaks increased with the laser power. The spectra presented peaks at 1306, 1063, 1001, 685, 646, 540, 527, 473, 384, 345, 300, 250, 215 and 168 cm^{-1} . Identification of lepidocrocite was clear, by the very narrow and intense 250 cm^{-1} peak. This iron compound presented other peaks at 1306, 646, 527, 384, 345, 300, 215 and 168 cm^{-1} . The peak at 384 cm^{-1} in the Raman spectrum was very intense, confirming the presence of another compound. This new phase was goethite with several peaks at 1306, 1063, 1001, 685, 540, 473, 384 (the most intense), 300, 250 and 215 cm^{-1} . Two iron compounds were detected for a wavelength of 633 nm while only goethite was observed for a wavelength of 532 nm.

At 0.25 mW small undefined peaks were observed in the spectrum of the dark regions on the steel surface, see Fig. 9(b). By increasing the laser power (from 2.5 to 25 mW) the peaks corresponding to goethite were intensified and clearly identified.

The spectra for the light and dark regions obtained with a lower laser energy (633 nm) did not present fluorescence and the iron compounds formed (goethite and lepidocrocite) were stable under laser heat.

In order to identify and locate the phases of the corrosion layers on the rebar, including those poorly crystallised, investigations with Raman micro-spectroscopy have been carried out in recent years. In such work the authors have always controlled the laser power, because some iron oxides are very sensitive to laser exposure. Bouchar et al. [28] used density filters to control the laser power on a sample under 100 μ W. Moreover, Singh et al. [29] observed that the Raman spectrum presented significant noise when a laser power of less than 1.5 mW was used. El Mendili et al. [30] investigated the stability of the γ -Fe₂O₃ nanoparticles under laser irradiation with laser powers from 0.08 to 48 mW on the sample and thermal treatment (300-1400°C). At 15 mW and 350°C the vibration modes of maghemite had vanished and low intensity bands attributed to the hematite phase appear in the Raman spectra. These vibration modes became stronger with increase of the laser power and the thermal treatment. Thus the laser power is a very important parameter when making measurements and it must also be taken into account that the laser output needs to be modified depending on the wavelength of the incident laser and the matrix studied.

Tables 2 and 3 show Raman peaks and the different iron corrosion products formed in each cementitious matrix with different laser powers using wavelengths of 532 and 633 nm. According to Chitty et al. [31] the corrosion system was made up of a multilayer structure constituted of a metallic substrate (M), a dense corrosion product

layer (DPL), a transformed medium (TM) and a binder (B). In the light of Raman results presented in this paper, different iron compounds and heterogeneous dense corrosion product layers (DPL) were observed on the steel extracted from alkali activated fly ash mortars. The type of iron phases formed was dependent on the type of alkaline solution used in the activation of fly ash and the amount of chloride added to the cementitious system, while the heterogeneous DPL was associated with the detection of two regions: dark and light. The difference in the colour of the rusts was associated with different thickness in the dense product layer. Previous authors also considered that the DPL thicknesses increased with the age of the sample, however in our case thickness depend on the aggressive solution. A higher thickness of DPL and detection of more crystalline compounds were observed in the dark areas. The corrosion products in the light regions were poor crystallized phases of iron oxyhydroxide while the products in the dark regions were goethite, except for FAB mortar in the presence of 0.4% Cl^- where lepidocrocite was formed. These results are in good agreement with precedent data published on dense corrosion product layer of steel embedded in concrete [5, 32]. However, neither Fe_3O_4 , FeO nor akaganeite were detected in these corrosion layers, no formation of the latter compound indicated that the amount of chlorine was not enough in the DPL to stabilise this phase. Additionally Hostis et al. [33] only found FeO , Fe_3O_4 as a thin layer before embedded in concrete and the corrosion phases formed were mainly iron oxyhydroxides (goethite).

Regarding the influence of the studied matrix (the type of alkaline solution used in the activation of fly ash), it should be remembered that the FA was activated with two alkaline solutions, one constituted only by NaOH (to manufacture FAA mortars) and other consisting of a mixture of NaOH and waterglass (to manufacture the FAB mortars). The matrix obtained with the solution containing a small amount of waterglass

(15%) was denser and more compact, and therefore chloride ion mobility to the steel surface was more hindered and the corrosion process was more restricted [34]. The iron corrosion products formed on the steel surface embedded in the FAB mortars were iron oxyhydroxides with low crystallinity, lepidocrocite and goethite, while poor crystallized phases of iron oxyhydroxides and goethite were detected in those formed on the FAA mortars. In addition, the aggressivity of the medium (the amount of chloride added to the cementitious system: 0.4 and 2% chlorides) also affected the nature of the corrosion products. In the FAB mortar with 0.4% chlorides (FAB0.4) with a dense matrix and lower amount of chlorides, slightly aggressive medium, lepidocrocite was formed.

The goethite present in the DPL is considered electrochemically stable. In contrast, lepidocrocite plays an active role in the corrosion mechanisms [35]. The dissolution of this phase in the wet stages is facilitated by slightly acidic media, leading to the dissolution of lepidocrocite and the precipitation of amorphous ferric oxyhydroxide upon drying. Finally, the amorphous ferric oxyhydroxide is transformed to goethite [36]. As such, the FAB mortar with 0.4% chlorides may be an insufficiently aggressive medium to promote the evolution of the rust in just 720 days, compared to the rest of the mortars, where the evolution of lepidocrocite to goethite has indeed taken place. Therefore, the characteristics of the cementitious matrices and the percentage of chloride ions influenced the nature of the iron phases.

Turning our attention to the influence of the incident laser wavelength on the iron corrosion products, the main objective of this work, well resolved Raman spectra could be obtained with laser powers between 0.025 and 0.25 mW for a wavelength of 532 nm (more energy) and with laser powers of 0.25 to 2.5 mW for a wavelength of 633 nm.

No peak or only small peaks were detected in Raman spectra obtained for the samples with both lasers at low power, 0.0005 mW with the 532 nm line and 0.25 mW with the 633 nm line. The attribution of these peaks was complicated.

The most important difference between the two wavelengths was associated with the stability of the iron corrosion products under laser heat during the tests. The phases formed: iron oxyhydroxides, goethite or lepidocrocite, were transformed into hematite or modified hematite at power equal to or above 0.5 mW using the laser line of 532 nm. For the laser with the high wavelength of 633 nm, the phases remained stable for all the conditions. Moreover, Raman spectra for the steel embedded in the four mortars obtained with the laser line 532 nm and high power (5 mW) showed fluorescence, leading to an increase in Raman intensity and a loss of peak definition of the corrosion products.

Conclusions

The main corrosion products generated on the surface of steel embedded in activated fly ash mortars in the presence of chlorides were poorly crystallised phases of iron oxyhydroxides, goethite (α -FeOOH) and lepidocrocite (γ -FeOOH).

The iron products formed should be studied with a laser line of 532 nm and a power from 0.025 to 0.25 mW or with a laser line of 633 nm and a power greater than 2.5 mW. The spectra obtained with the 532 nm line and 0.0005 mW or with the 633 nm line and 0.25 mW presented low resolution, no peak or only small peaks were detected.

For the wavelength of 532 nm the phases formed: oxyhydroxides with low crystallinity, goethite and lepidocrocite, were transformed into hematite or modified hematite at a power equal to or above 0.5 mW. The spectra recorded with this line with 5 mW showed fluorescence.

Acknowledgements

M. Criado expresses her gratitude to the Spanish Ministry of Science and Innovation for her Juan de la Cierva contract (Ref. JDC–2010). The authors express their gratitude to Project BIA2008–05398 from CICYT, Spain, for financial support. The authors also thank the European Community and Comunidad de Madrid for supporting two Geomateriales programs (S2013/MIT–2014).

References

1. Zitrou E, Nikolaou J, Tsakiridis PE, Papadimitriou GD. Atmospheric corrosion of steel reinforcing bars produced by various manufacturing processes. *Constr Build Mater* 2007;21:1161–9.
2. Almusallam AA. Effect of degree of corrosion on the properties of reinforcing steel bars. *Constr Build Mater* 2001;15:361–8.
3. González JA, Miranda J. Corrosión en las Estructuras de Hormigón Armado: Fundamentos, Medida, Diagnóstico y Prevención. Consejo Superior de Investigaciones Científicas, 30, Madrid: Biblioteca de Ciencias; 2007.
4. Poupard O, L’Hostis V, Catinaud S, Petre-Lazar I. Corrosion damage diagnosis of a reinforced concrete beam after 40 years natural exposure in marine environment. *Cement Concrete Res* 2006;36:504–20.
5. L’Hostis V, Neff D, Bellot-Gurlet L, Dillmann P. Characterization of long-term corrosion of rebars embedded in concretes sampled on French historical buildings aged from 50 to 80 years. *Mater Corros* 2009;60:93–8.
6. Ahmad S. Reinforcement corrosion in concrete structures, its monitoring and service life prediction—a review. *Cement Concrete Comp* 2003;25:459–71.
7. Criado M, Martínez-Ramírez S, Fajardo S, Gómez PP, Bastidas JM. Corrosion rate and corrosion product characterisation using Raman spectroscopy for steel embedded in chloride polluted fly ash mortar. *Mater Corros* 2013;64:372–80.

8. Ghods P, Isgor OB, Burkan O, Bensebaa F, Kingston D. Angle-resolved XPS study of carbon steel passivity and chloride-induced depassivation in simulated concrete pore solution. *Corros Sci* 2012;58:159–67.
9. Aperador W, Mejía de Gutiérrez R, Bastidas DM. Steel corrosion behaviour in carbonated alkali-activated slag concrete. *Corros Sci* 2009;51:2027–33.
10. Mohammadi F, Nickchi T, Attar MM, Alfantazi A. EIS study of potentiostatically formed passive film on 304 stainless steel. *Electrochim Acta* 2011;56:8727–33.
11. Fajardo S, Bastidas DM, Ryan MP, Criado M, McPhail DS, Bastidas JM. Low-nickel stainless steel passive film in simulated concrete pore solution: A SIMS study. *Appl Surf Sci* 2010;256:6139–43.
12. Souier T, Martin F, Bataillon C, Cousty J. Local electrical characteristics of passive films formed on stainless steel surfaces by current sensing atomic force microscopy. *Appl Surf Sci* 2010;256:2434–9.
13. Larroumet D, Greenfield D, Akid R, Yarwood J. Raman spectroscopic studies of the corrosion of model iron electrodes in sodium chloride solution. *J Raman Spectrosc* 2007;38:1577–85.
14. Chen W, Du R-G, Ye C-Q, Zhu Y-F, Lin C-J. Study on the corrosion behavior of reinforcing steel in simulated concrete pore solutions using in situ Raman spectroscopy assisted by electrochemical techniques. *Electrochim Acta* 2010;55:5677–82.
15. Dubois F, Mendibide C, Pagnier T, Perrard F, Duret C. Raman mapping of corrosion products formed onto spring steels during salt spray experiments. A correlation between the scale composition and the corrosion resistance. *Corros Sci* 2008;50:3401–9.

- 399 16. Baek W-C, Kang T, Sohn H-J, Kho YT. In situ surface enhanced Raman
400 spectroscopic study on the effect of dissolved oxygen on the corrosion film on
401 low carbon steel in 0.01 M NaCl solution. *Electrochim Acta* 2001;46:2321–5.
- 402 17. Neff D, Bellot-Gurlet L, Dillmann P, Reguer S, Legrand L. Raman imaging of
403 ancient rust scales on archaeological iron artefacts for long-term atmospheric
404 corrosion mechanisms study. *J Raman Spectrosc* 2006;37:1228–37.
- 405 18. L’Hostis V, Amblard E, Guillot W, Paris C, Bellot-Gurlet L. Characterisation of
406 the steel concrete interface submitted to chloride-induced-corrosion. *Mater*
407 *Corros* 2013;64:185–94.
- 408 19. Colomban P, Cherifi S, Despert G. Raman identification of corrosion products on
409 automotive galvanized steel sheet. *J Raman Spectrosc* 2008;39:881–6.
- 410 20. de Faria DLA, Venancio-Silva S, de Oliveira MT. Raman microspectroscopy of
411 some iron oxides and oxyhydroxides. *J Raman Spectrosc* 1997;28:873–8.
- 412 21. Nieuwoudt MK, Comins JD, Cukrowski I. The growth of the passive film on iron
413 in 0.05 M NaOH studied in situ by Raman micro-spectroscopy and
414 electrochemical polarisation. Part I: near-resonance enhancement of the Raman
415 spectra of iron oxide and oxyhydroxide compounds. *J Raman Spectrosc*
416 2011;42:1335–9.
- 417 22. Bernal SA, Provis JL. Durability of Alkali-Activated Materials: Progress and
418 Perspectives. *J Am Ceram Soc* 2014;97:997–1008.
- 419 23. UNE 80–225–93 Spanish Standard, Test method for cements: chemical analysis.
420 Determination of the reactive silica (SiO_2) content in cements, pozzolans and fly
421 ashes;1993.

24. Arjuman P, Silbee MR, Roy DM. Quantitative determination of the crystalline and amorphous phases in low calcium fly ash. Ed. H. Justnes, In: Proc. 10thICCC Gothenburg, Sweden; 1997:3v 020 4.
25. Criado M, García-Díaz I, Bastidas JM, Alguacil FJ, López FA, Monticelli C. Effect of recycled glass fiber on the corrosion behavior of reinforced mortar. *Constr Build Mater* 2014;64:261–9.
26. Nauer G, Strecha P, Brinda-Konopikand N, Liptay G. Spectroscopic and thermoanalytical characterization of standard substances for the identification of reaction products on iron electrodes. *J Therm Anal* 1985;30:813–30.
27. Froment F, Tournié A, Colomban P. Raman identification of natural red to yellow pigments: ochre and iron-containing ores. *J Raman Spectrosc* 2008;39:560–8.
28. Bouchar M, Foy E, Neff D, Dillman P. The complex corrosion system of a medieval iron rebar from the Bourges. *Corros Sci* 2013;76:361–72.
29. Singh JK, Singh DDN. The nature of rusts and corrosion characteristics of low alloy and plain carbon steels in three kinds of concrete pore solution with salinity and different pH. *Corros Sci* 2012;56:129–42.
30. El Mendili Y, Bardeau J-F, Randrianantoandro N, Grasset F, Greneche J-M. Insights into the mechanism related to the phase transition from γ -Fe₂O₃ to α -Fe₂O₃ nanoparticles induced by thermal treatment and laser irradiation. *J Phys Chem C* 2012;116:23785-23792.
31. Chitty W-J, Dillmann P, L'Hostis V, Lombard C. Long-term corrosion resistance of metallic reinforcements in concrete—a study of corrosion mechanisms based on archaeological artefacts. *Corros Sci* 2005;47:1555–81.

32. Duffó GS, Reinoso M, Ramos CP, Farina SB. Characterization of steel rebars embedded in a 70-year old concrete structure. *Cement Concrete Res* 2012;42:111–7.
33. L’Hostis V, Foct F, Dillmann P. Corrosion behaviour of reinforced concrete: Laboratory experiments and archaeological analogues for long-term predictive modelling. *J Nucl Mater* 2008;379:124–32.
34. Criado M, Bastidas DM, Fajardo S, Fernández-Jiménez A, Bastidas JM. Corrosion behaviour of a new low-nickel stainless steel embedded in activated fly ash mortars. *Cement Concrete Comp* 2011;33:644–52.
35. Monnier J, Bellot-Gurlet L, Baron D, Neff D, Guillot I, Dillmann P. A methodology for Raman structural quantification imaging and its application to iron indoor atmospheric corrosion products. *J Raman Spectrosc* 2011;42:773–781.
36. Misawa T, Asami K, Hashimoto K, Shimodaira S. The mechanism of atmospheric rusting and the protective amorphous rust on low alloy steel. *Corr. Sci.* 1974;14:279-89.

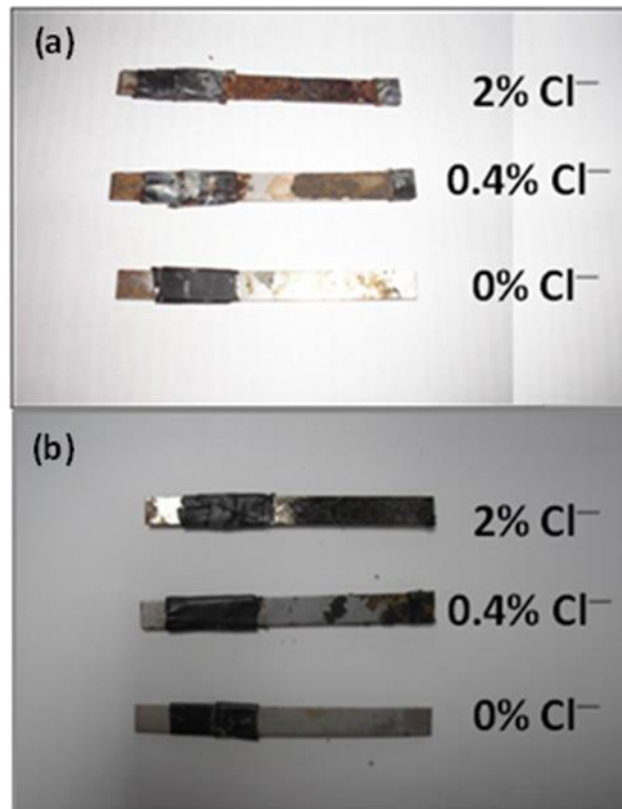
FIGURES

Fig. 1. Steel specimens extracted from the (a) FAA and (b) FAB mortars without chlorides and with 0.4 and 2% chlorides after 720 days of experimentation.

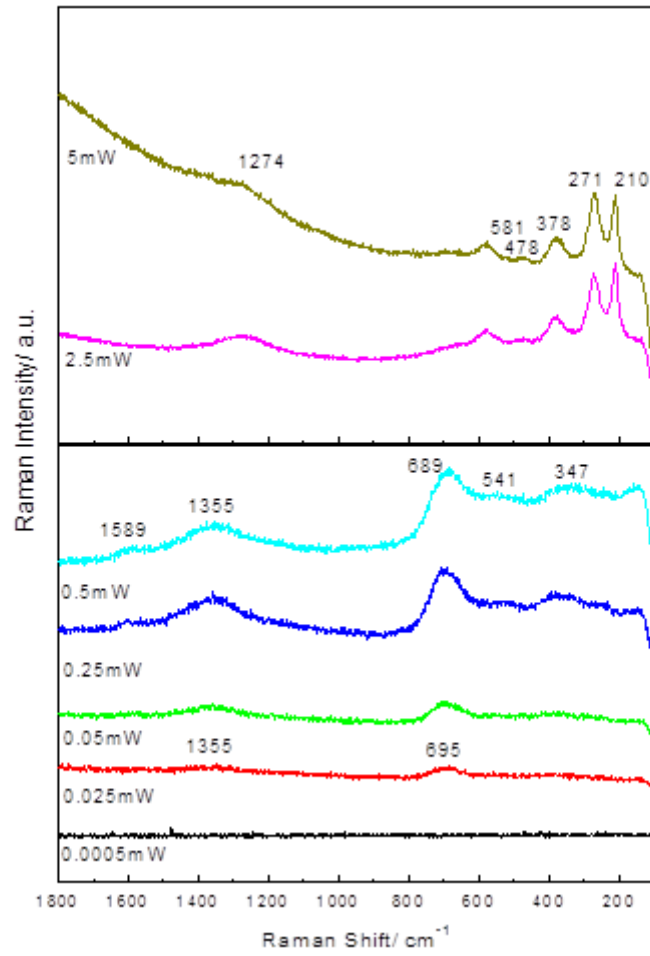


Fig. 2. In situ Raman spectra of the corroded bar embedded in FAA mortar with 0.4% chlorides using an optimised excitation wavelength of 532 nm under different laser output power.

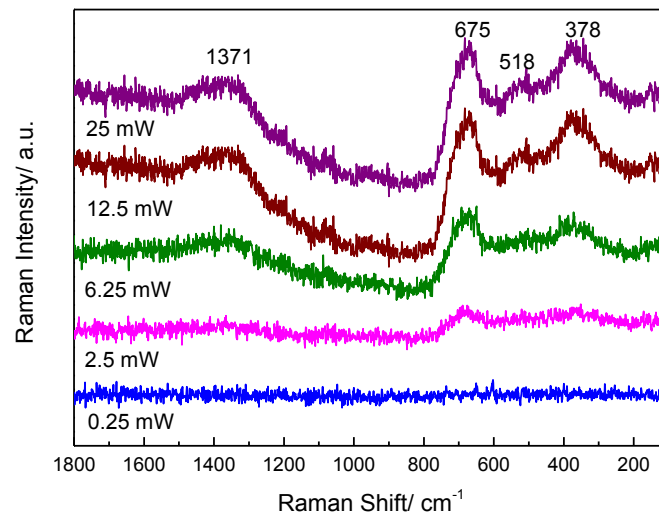


Fig. 3. In situ Raman spectra of the corroded bar embedded in FAA mortar with 0.4% chlorides using an optimised excitation wavelength of 633 nm under different laser output power.

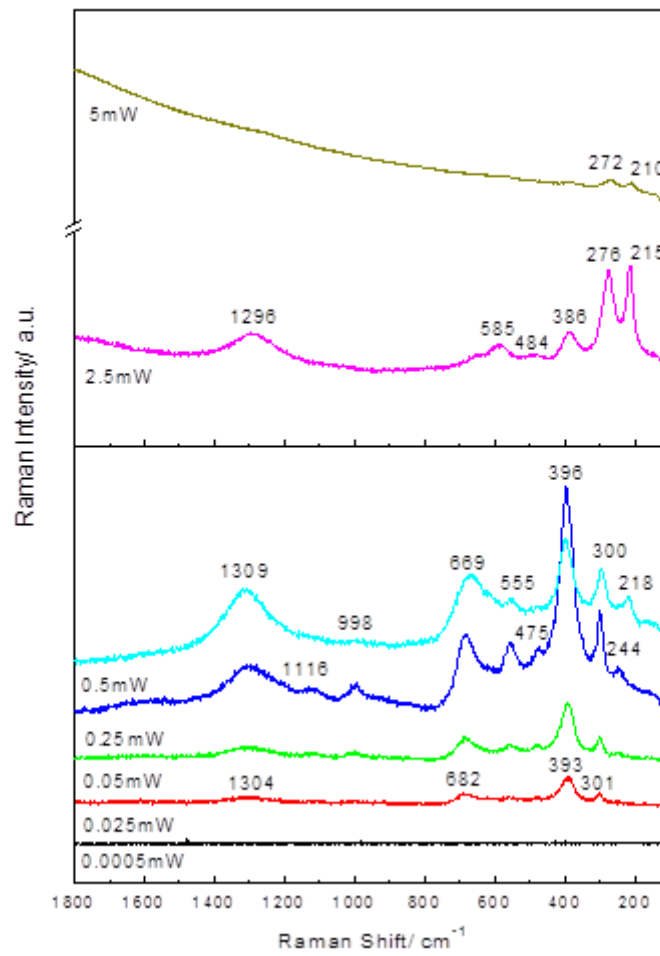


Fig. 4. In situ Raman spectra of the corroded bar embedded in FAA mortar with 2% chlorides using an optimised excitation wavelength of 532 nm under different laser output power.

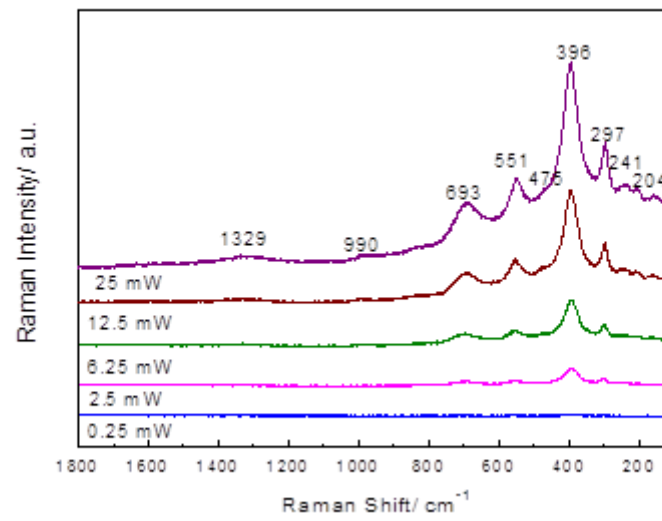


Fig. 5. In situ Raman spectra of the corroded bar embedded in FAA mortar with 2% chlorides using an optimised excitation wavelength of 633 nm under different laser output power.

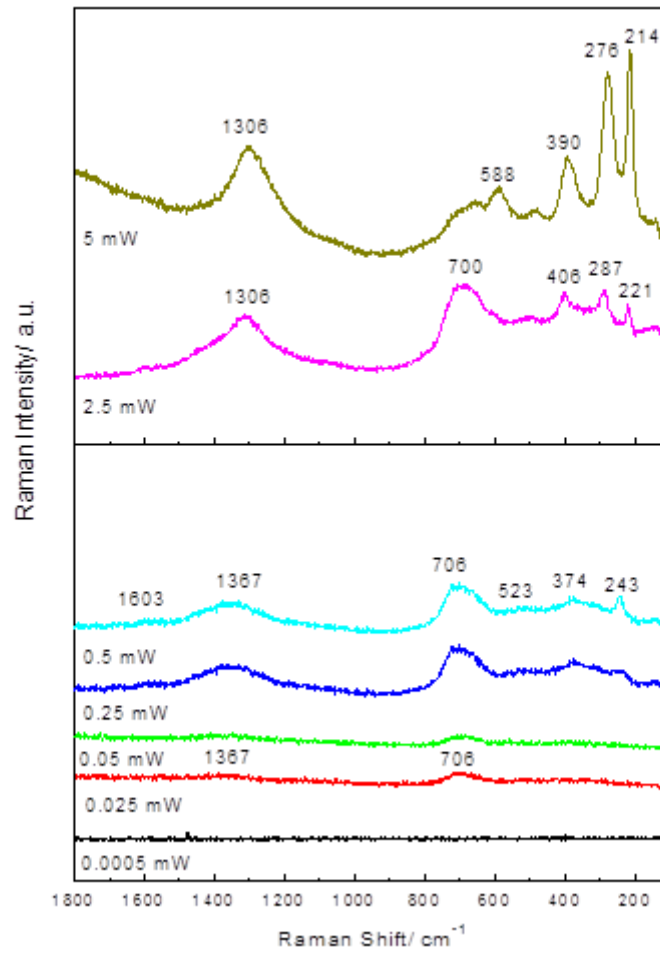


Fig. 6. In situ Raman spectra of the corroded bar embedded in FAB mortar with 0.4% chlorides using an optimised excitation wavelength of 532 nm under different laser output power.

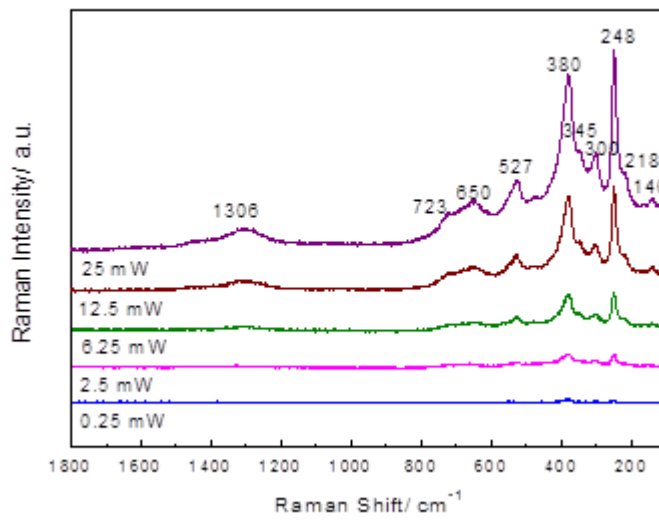


Fig. 7. In situ Raman spectra of the corroded bar embedded in FAB mortar with 0.4% chlorides using an optimised excitation wavelength of 633 nm under different laser output power.

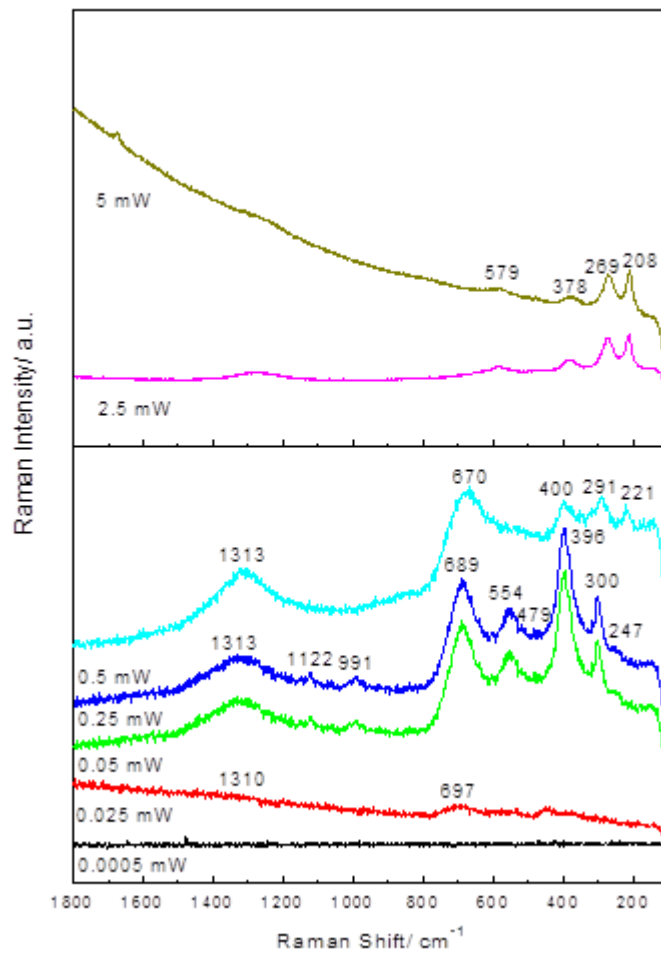


Fig. 8. In situ Raman spectra of the corroded bar embedded in FAB mortar with 2% chlorides using an optimised excitation wavelength of 532 nm under different laser output power.

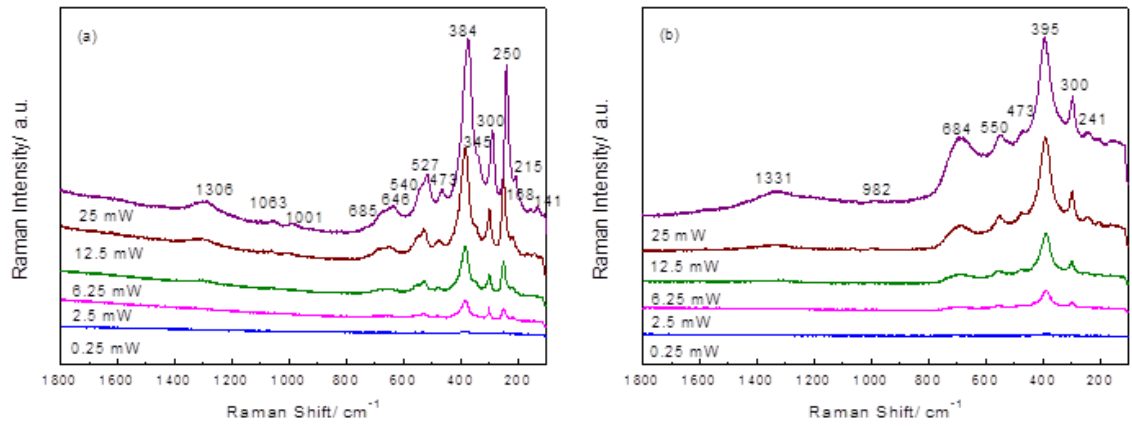


Fig. 9. In situ Raman spectra of the corroded bar embedded in FAB mortar with 2% chlorides using an optimised excitation wavelength of 633 nm under different laser output power, (a) light and (b) dark regions.

557

558 Table 1. Chemical composition of the tested fly ash (% mass).

559

SiO ₂	Al ₂ O ₃	Fe ₂ O ₃	CaO	MgO	SO ₃	Na ₂ O	K ₂ O	MnO	P ₂ O ₅	TiO ₂	LOI	Others	Total
51.78	27.80	6.18	4.59	1.52	0.71	0.59	2.51	0.06	0.62	1.35	2.23	0.06	100
560	LOI: Loss on ignition												
561													
562													

Table 2. Raman peaks and main phases identified in FAA mortar with the different powers for the wavelengths of 532 and 633 nm.

Frequency (cm ⁻¹)	FAA mortar						
	$\lambda = 633 \text{ nm}$		$\lambda = 532 \text{ nm}$				
	0.4%	2%	0.4%		2%		
	0.25mW- 25mW	0.25mW- 25mW	0.05mW- 0.5mW	2.5mW- 5mW	0.025mw- 0.05mW	0.25mW- 0.5mW	2.5mW- 5mW
693 684 675 669 650	b	m,b	b		w,b	m,b	
581 550 540 527 518	b	m	w, b	m	m,b	m,b	m
475		sh		w		w	w
396 380 345 300 272 244 215	b	s m	w,b	m s s	s m	s m m	m,b s s
Identified phases	O; G [13,17,18, 21, 27]	O; G [13,17,18, 21, 27]	O; G [13,17,18, 21, 27]	M.H.	G [13,18, 21, 27]	G; M.H [13,18, 21, 27]	M.H

s: strong; m: medium; b: broad; w: weak; sh: sharp

O: iron oxyhydroxides with low crystallinity; G = Goethite; M.H. Modified Hematite;

Table 3. Raman peaks and main phases identified in FAB mortar with the different powers for the wavelengths of 532 and 633 nm.

Frequency (cm ⁻¹)	FAB mortar									
	$\lambda = 633$ nm			$\lambda = 532$ nm						
	0.4%	2%		0.4%			2%			
	0.25mW-25mW	Dark region	Ligh region	0.025mW-0.5mW	2.5mW	5mW	0.025mW	0.05mW-0.25mW	0.5mW	2.5mW-5mW
706				m,b	s,b	m,b				
693							b	m		
684		m,b	m,b							
675	m								m	
650			m,b							
588						m,b				m,b
579										
559								m		
550		m								
540	m		m							
527			m							
518										
475		sh	w				b			
396		s	s		m	m		s	m	m,b
380	s		s							
374				w						
345	sh		sh							
300		s	s					s		
287					m				m	
270						s				s
248		w	s	w						
221					m				m	
214						s				s
Identified phases	L [13,17,18]	G; L [13,17,18,21,27]	G; L [13,17,18,21,27]	O; L [13,17,18,21,27]	H [19]	M.H	O [17,18]	G [13,17,18,21,27]	H [19]	M.H

s: strong; m: medium; b: broad; w: weak; sh: sharp

L: Lepidocrocite; O: iron oxyhydroxides with low crystallinity; G = Goethite; M.H.

Modified Hematite